Observation of the Fano Resonance in Gold Nanorods Supported on High-Dielectric-Constant Substrates

Huanjun Chen,[†] Lei Shao,[†] Tian Ming,[†] Kat Choi Woo,[†] Yat Cho Man,[†] Jianfang Wang,[†,*] and Hai-Qing Lin[†,‡,*]

[†]Department of Physics, The Chinese University of Hong Kong, Shatin, Hong Kong SAR, and [‡]Beijing Computational Science Research Center, Beijing 100084, China

ABSTRACT Fano resonances in plasmonic nanostructures, characterized by their asymmetric resonance spectral profile, are currently attracting much interest due to their potential applications in biological sensing, metamaterials, photoswitching, and nonlinear optical devices. In this study, we report on the observation of the Fano resonance in Au nanorods induced by their coupling with the supporting substrate. For Au nanorods having a large size and deposited on a substrate with a large dielectric constant, the strong nanorod–substrate coupling gives rise to a Fano line shape on the far-field scattering spectrum. Electrodynamic calculations reveal that the Fano resonance originates from the interference of a broad octupolar and a narrow quadrupolar plasmon mode of the nanorod. Such an interaction is enabled by the strong image charges induced by substrates with high dielectric constants. Moreover, the Fano resonance is very sensitive to the nanorod–substrate spacing. When the spacing is experimentally increased to be larger than ~8 nm, the Fano resonance disappears. These results will be important not only for understanding the interference of different plasmon modes in plasmonic systems but also for developing a number of plasmon-based optical and optoelectronic devices.

KEYWORDS: dielectric function · Fano resonance · gold nanorod · plasmon resonance · scattering · substrate

Since its discovery in 1801 by Tomas Young,[1] interference has been a very important fundamental subject in both theories and experiments. In most cases, interference refers to the coherent interaction between two spectrally overlapping oscillations or resonances. Specifically, the interference between a broad resonance and a narrow one can give rise to a distinctly asymmetric resonance line shape. This newly generated line shape cannot be described by the traditional Lorentzian formula. This type of interference is termed as Fano resonance. It bears the name of Ugo Fano, who first suggested its theoretical description.[2] Fano resonances are generally regarded as the result of the destructive interference between a broad and a narrow resonance mode. Such a destructive interaction suppresses the amplitude near the frequency of the narrow mode and gives rise to a spectrum characterized by an asymmetric shape or sometimes a distinct dip structure.[2–5] Due to their increasing importance in revealing the underlying physics in different disciplines, more and more efforts have been devoted to the investigation of Fano resonances. Over the past few decades, Fano resonances have been ubiquitously observed in atomic physics,[2,6,7] optics,[8–11] condensed matter physics,[12–15] and electronic circuits.[3]

Metal nanostructures exhibiting Fano resonances in their optical responses have recently received much attention owing to the rapid progress in the fabrication and characterization techniques.[4,5] They exhibit rich localized plasmon resonances that originate from the collective electron oscillations confined at the nanoscale. Different plasmon modes can be supported in a single metal nanostructure. They are manifested as peaks on the extinction or scattering spectra. Depending on their decay channels, these modes have different line widths. Broad dipolar plasmon modes can efficiently couple with the external electromagnetic field through radiative decays and are therefore often named as "bright modes". On the contrary, for narrow modes with small net dipole moments, their radiative decays are very weak. They are often termed as "dark mode".[16–18] The presence of both bright and dark modes forms the essential basis for the Fano resonances in metal nanostructures. Theories have predicted that a single solid metallic sphere can exhibit a strong Fano resonance due to the interference between its dipole and quadrupole modes.[5,19] Intrinsic Fano resonances have been observed in palladium nanodisks owing to the coupling between the dipolar plasmon mode and the interband transition background of palladium.[20] Multilayer core–shell nanostructures have been designed with spectrally overlapping bright and dark modes, resulting in a Fano

* Address correspondence to jfwang@phy.cuhk.edu.hk, hqlin@phy.cuhk.edu.hk.

Received for review June 23, 2011 and accepted July 25, 2011.

Published online July 25, 2011
10.1021/nn202317b

resonance in their scattering spectra.[21] Complex coupled metallic nanostructures have been demonstrated to exhibit intriguing Fano resonances, which originate from the rich plasmon hybridization of the different plasmon modes in each unit, such as disk–ring cavities,[17,18,22] self-assembled metal nanostructure heptamers and quadrumers,[23–27] Au dolmen structures,[28,29] and intricately shaped Au heterostructures.[30,31] Apart from their fundamental physical interests, Fano resonances in metal nanostructures are of great potential in a range of applications. The most straightforward one is chemical and biological sensing. The narrower line widths produced by Fano resonances can lead to plasmonic sensors with very large figures of merit, which are defined as the refractive index sensitivities divided by the resonance line widths. Such plasmonic sensors have been proposed in ring–disk nanocavities,[17,22] which exhibit figures of merit in the range of 3–8. The destructive interference nature of plasmonic Fano resonances can strongly suppress the radiative damping and be utilized for the fabrication of metamaterials with very narrow and nearly full transparency windows.[32] Furthermore, metal nanostructures with Fano resonances can be employed for various active optoelectronic applications, such as switching and electro-optical modulation.[33,34] Studying and realizing Fano resonances in metal nanostructures are therefore very important not only for furthering our understanding on light–matter interactions at the nanoscale but also for the design of various plasmonic optical and optoelectronic devices.

One means for realizing Fano resonances in plasmonic metal nanostructures is the introduction of symmetry breaking into the system. Symmetry breaking can enable the hybridization of different plasmon modes and therefore lead to the effective coupling between broad and narrow plasmon resonances. The most straightforward approach for symmetry breaking is to make hybrid metal nanostructures geometrically asymmetric. Nonconcentric Au ring–disk nanocavities have been shown to exhibit strong and tunable Fano resonances in the near-infrared range.[17,18,22] A similar phenomenon has also been observed in multilayer Au nanoshell structures, in which the center of the core is displaced with respect to the center of the entire system.[21] Symmetry breaking can also be achieved in heterodimers that are composed of different metals.[35,36] In such heteronanostructures, the Fano line shape as well as its resonance position can be readily tailored by controlling the geometrical parameters of the two metallic components. One common feature among the metal nanostructures mentioned above is that they are fabricated by use of complex, multistep, and expensive lithographic techniques. The use of complex lithographic techniques hinders the large-scale applications of metal nanostructures.

Another approach for symmetry breaking has recently been proposed. In this approach, metal nanocrystals are deposited on dielectric or metal substrates. The presence of substrates brings a non-uniform dielectric environment around the nanocrystal, which leads to the excitation of the multipolar plasmon modes. The electron oscillations associated with these modes can induce image charges in the substrate, which can in turn interact with the excited plasmon modes in the nanocrystal. As a result, the substrate mediates the interactions among the different plasmon modes of the nanocrystal and causes their hybridization.[37–40] In this regard, Fano resonances are more likely to be observed when metal nanocrystals of large sizes are deposited on substrates with high dielectric constants. Substrates with high dielectric constants can induce stronger image charges, while the excitation of multipolar plasmon modes is more effective in larger nanocrystals owing to the retardation effect. Both of these effects are essential for initiating the hybridization among different plasmon modes. The symmetry breaking caused by supporting substrates is simple and does not need expensive fabrication techniques. Up to date, several theoretical studies have predicted the presence of Fano resonances in metal nanocrystals that are deposited on substrates with high dielectric constants.[37,41] On the other hand, the asymmetric line shapes implying the presence of Fano resonances have been observed indirectly in a few experiments on supported metal nanocrystals, but no careful and conclusive analyses regarding Fano resonances have been provided.[40,42] In both of these previous theoretical and experimental studies, only metal nanostructures of high symmetries, such as nanoshells and nanocubes, have been considered. Elongated metal nanocrystals are known to exhibit synthetically tunable scattering cross sections and plasmon resonance wavelengths, large local electric field enhancements, and strongly suppressed plasmon damping.[43–46] Elongated metal nanocrystals are therefore expected to exhibit intriguing and controllable Fano resonances.

Here we report on the experimental observation of Fano resonances in Au nanorods that are supported on substrates by carefully examining the scattering spectra from Au nanorods of different volumes deposited on substrates with different dielectric functions. Our studies show that substrates with large dielectric constants can effectively mediate the hybridization between the different plasmon modes in a supported Au nanorod. Specifically, the coupling between the quadrupolar and octupolar resonances in a large Au nanorod can produce a Fano resonance, which is characterized by a dip structure in the scattering spectrum. Moreover, the Fano resonance is found to be strongly dependent on the spacing between the nanorod and substrate. It only takes effect when the spacing is smaller than ~8 nm.

RESULTS AND DISCUSSION

Our studies were carried out at the single-particle level on a dark-field scattering microscope. The excitation white light was transmitted through a 100× dark-field

objective with a numerical aperture of 0.80. The light through the objective has an incident angle of 53°. It has both p- and s-polarizations. For p-polarized excitation, the incident electric field can be decomposed into two components. One is perpendicular [vertical (V) excitation], and the other is parallel to the substrate plane (Figure 1). The parallel component can be further decomposed according to the nanorod length axis into the field that is oriented along the nanorod length axis [horizontal and longitudinal (HL) excitation] and the one that is oriented perpendicular to the nanorod length axis [horizontal and transverse (HT) excitation]. For s-polarized excitation, the incident electric field consists only of the HL and HT components. The optical response of a Au nanorod is determined by the specific excitation manner.

The Au nanorods used in our experiments were prepared using a seeded growth method in conjunction with anisotropic oxidation.[44,47,48] Cetyltrimethylammonium bromide (CTAB) surfactant was employed as the stabilizing agent. We first examined the plasmonic properties of small Au nanorods that were deposited on different dielectric substrates. Figure 2a shows the scanning electron microscopy (SEM) image of the small nanorod sample. The size and shape distributions of this sample are highly uniform. The average diameter, length, and aspect ratio are determined to be 42 ± 3 nm, 89 ± 7 nm, and 2.1 ± 0.2, respectively. Two types of substrates were utilized. They are cover glass slides with a small dielectric constant of 2.40 at 600 nm and silicon wafers with a large dielectric constant of 15.6 at 600 nm.[49] The dielectric constant of silicon should be a complex number. However, due to the much smaller value of the imaginary part, ~0.2 at 600 nm, we omitted it and only considered its real part in our following discussion. After the nanorods were washed twice by centrifugation to remove the excess surfactant, they were deposited by immersing the substrates in the nanorod solution for a controlled period of time and then blowing them dry with nitrogen. The number density of the nanorods on each substrate was controlled to be 1−3 per μm^2. The nanorods are capped with a CTAB bilayer. The thickness of the bilayer has been measured to be ~1.5 nm.[50] Because of the flexibility of the CTAB molecules, the spacing between the nanorods and substrate is expected to be less than 1.5 nm.

Figure 2b shows the representative scattering spectra of the individual small Au nanorods that are supported on a glass slide. Each small nanorod exhibits only one dominant scattering peak, which is located at 580 nm and has a line width of 57 nm. In contrast, when the small nanorods are supported on silicon, their scattering spectra show two resonance peaks (Figure 2c). One is positioned at 530 nm and the other at 680 nm. Numerical electrodynamic calculations using the finite-difference time-domain method (FDTD) were performed in order to ascertain the origins

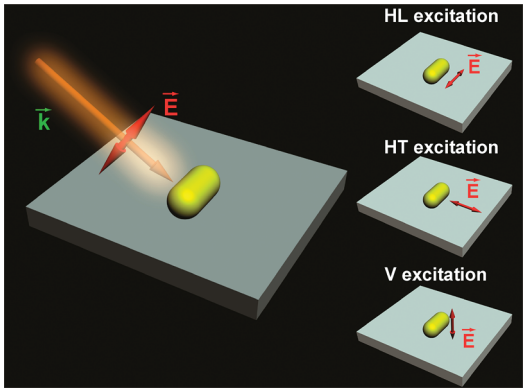

Figure 1. Schematic showing the different excitation manners. Left: single Au nanorod is illuminated by a white light source at an oblique incidence angle. Right: top shows the excitation light polarized horizontally and along the nanorod length axis; the middle shows the excitation light polarized horizontally and perpendicular to the nanorod length axis; and the bottom shows the excitation light polarized vertically.

of these resonance peaks. In accordance with the excitation scheme shown in Figure 1, the different excitation polarizations were considered (Figure 2b,c, colored curves). The scattering intensities under the V and HT excitation polarizations are very small for the small nanorod on the glass substrate. The HL-excited plasmon resonance peak dominates the total scattering spectrum. A free-standing Au nanorod in a uniform surrounding dielectric medium generally possesses a longitudinal and a transverse intrinsic plasmon resonance mode, which are polarized along and perpendicular to the nanorod length axis, respectively. The scattering intensity of the longitudinal mode is much stronger than that of the transverse one.[51] The above result indicates that the plasmonic properties of the small Au nanorod remain nearly unchanged in the presence of the glass substrate. This can be ascribed to the small dielectric constant of the glass substrate. The image charges produced in the glass substrate are not strong enough.

In contrast, when the small nanorods are deposited on the silicon substrate, the V-excited plasmon peak is strongly enhanced, with its scattering intensity comparable to that of the HL-excited plasmon peak (Figure 2c). In addition, the HL-excited plasmon peak shows a red shift of ~100 nm relative to that of the nanorod on the glass substrate. These results are ascribed to the much larger dielectric constant of silicon than that of glass. A large difference in the dielectric constant at the substrate−air interface produces larger image charges in the substrate, which leads to the strong coupling between the plasmon resonances in the nanorod and the image charges in the substrate. As the oscillation of the induced image charges is out of phase with that of the HL-excited plasmon mode, the restoration force of the HL-excited plasmon mode is reduced. Its resonance wavelength is

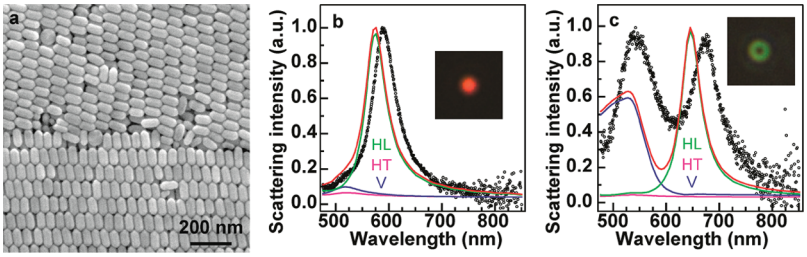

Figure 2. (a) SEM image of the small Au nanorod sample. (b) Experimental (black circles) and calculated (colored curves) scattering spectra of an individual small Au nanorod supported on the glass substrate. (c) Experimental (black circles) and calculated (colored curves) scattering spectra of an individual small Au nanorod supported on the silicon substrate. The green, pink, and blue curves represent the spectra obtained under the HL, HT, and V polarization scheme, respectively. The red curve represents the sum of the three curves. The colored images in the insets are the far-field scattering patterns of the corresponding individual nanorods. The experimental scattering spectra of over 20 nanorods were taken on each substrate. They are similar to one another. Shown here are representative ones.

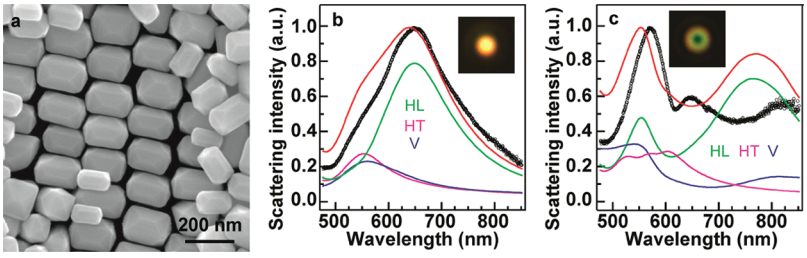

Figure 3. (a) SEM image of the large Au nanorod sample. (b) Experimental (black circles) and calculated (colored curves) scattering spectra of an individual large Au nanorod supported on the glass substrate. (c) Experimental (black circles) and calculated (colored curves) scattering spectra of an individual large Au nanorod supported on the silicon substrate. The green, pink, and blue curves represent the spectra obtained under the HL, HT, and V excitation polarization scheme, respectively. The red curve represents the sum of the three curves. The colored images in the insets are the far-field scattering patterns of the corresponding individual nanorods. The experimental scattering spectra of over 20 nanorods were taken on each substrate. They are similar to one another. Shown here are representative ones.

therefore red-shifted. For the V-excited plasmon mode, the oscillation of the induced image charges in the substrate is in phase with that of the plasmon mode in the nanorod. The net restoration force is therefore largely enhanced in comparison to the case of the nanorod supported on glass. As a result, the scattering intensity of the nanorod on silicon under the V excitation polarization is much stronger than that of the nanorod on glass. In addition, the scattering pattern of the nanorod on silicon assumes a doughnut shape, while that of the nanorod on glass appears as a solid spot (Figure 2b,c insets and Figure S1a,c, Supporting Information). The difference in the scattering pattern can be attributed to the dependence of the net dipole strength of the V-excited plasmon mode on the substrate dielectric constant. We have systematically investigated the effect of various substrates on the scattering patterns of supported Au nanorods in our recent study.[52] The HT-excited plasmon mode of the nanorods on silicon is very weak, which is similar to the case of the small nanorods supported on glass. For both types of substrates, the total scattering spectra are sums of the spectra calculated under the HL, HT, and V excitation polarizations. There is no interference among the different plasmon modes. The small size of the nanorods precludes the excitation of the multipolar plasmon modes. The above results and analyses show that Fano resonances cannot be observed in small Au nanorods *via* the symmetry breaking caused by a substrate, even though the introduced substrate has a very large dielectric constant.

On the basis of the above results, we then chose large Au nanorods and measured their scattering spectra. The large nanorod sample was prepared by a modified seeded growth method, as described in our previous study.[53] The average diameter, length, and aspect ratio are measured to be 118 ± 7 nm, 188 ± 5 nm, and 1.6 ± 0.1, respectively (Figure 3a). The average particle volume is ~17 times that of the small nanorod sample. When supported on the glass substrate, the large Au nanorods exhibit a scattering peak with a line width of 120 nm (Figure 3b). This scattering peak is much broader than that of the small ones. FDTD calculations indicate that the total scattering spectrum is dominated by the HL-excited plasmon mode at 658 nm. This is also consistent with the observation of a solid bright scattering spot (Figure 3b inset and Figure S1b, Supporting Information) because the HL-excited plasmonic dipole is oriented parallel to the substrate plane.[52] The broadening of the HL-excited plasmon mode is due to the increase of the radiation damping as the nanorod becomes larger. Our experimental and simulated scattering spectra indicate that the interference among the different plasmon

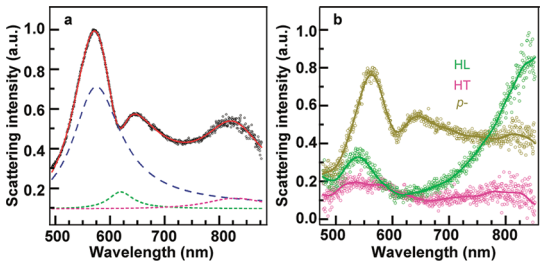

Figure 4. (a) Fitting the scattering spectrum of an individual large Au nanorod supported on the silicon substrate with the Fano interference model. The used parameters are a_r = −0.34, b_1 = 0.29, Γ_1 = 0.09 eV (28 nm), ϕ_1 = 1.28π, E_1 = 2.00 eV (620 nm); b_2 = 0.78, Γ_2 = 0.20 eV (54 nm), ϕ_2 = 0.58π, E_2 = 2.15 eV (577 nm); b_3 = 0.23, Γ_3 = 0.12 eV (92 nm), ϕ_3 = 0.39π, E_3 = 1.49 eV (832 nm). The red line is the fitting result using these parameters. The black circles represent the experimental spectrum. The green, blue, and pink dashed curves are the contributions from the three resonances. (b) Experimental scattering spectra acquired under the HL (green), HT (pink), and p- (yellow) excitation polarization schemes. The p-excitation polarization for this particular nanorod consists of both the HL and V components. The solid curves are guides for eyes.

modes still cannot be observed for the large Au nanorods supported on substrates with small dielectric constants.

The scattering spectra are enriched when the large nanorods are deposited on the silicon substrate. Three separate scattering peaks are observed, as shown in Figure 3c. They are centered at 580, 650, and 830 nm, respectively. What is more interesting is that a well-defined small dip is clearly seen between the two high-energy peaks. Such a dip structure on a broad spectrum is a clear indication of the appearance of a Fano resonance.[21,29,41] The simulation results show that two plasmon modes are excited under the HL polarization. One is broad and centered at 770 nm, and the other is narrow and centered at 560 nm. Their widths are 139 and 39 nm, respectively. From the discussion below, the broad resonance can be assigned to a dipolar plasmon mode, and the narrow one is a quadrupolar mode due to the large size of the nanorod and the large dielectric constant of silicon. The V excitation polarization gives a relatively broad and intense resonance peak at 540 nm with a line width of 84 nm. This peak suggests that the coupling in the vertical direction between the plasmon in the large nanorod and the image charges in the silicon substrate is very strong. The strong coupling in the vertical direction is also verified by the doughnut-shaped scattering pattern (Figure 3c inset and Figure S1d, Supporting Information) because the V-excited net plasmonic dipole is oriented perpendicular to the substrate.[52] The HT-excited plasmon mode is very broad. It can be considered as a background over the spectral region around the dip structure. The scattering spectra obtained from the simulations under the three different excitation polarization schemes are then linearly added together. A comparison of the total scattering spectrum (Figure 3c, red curve) with the measured one indicates that the calculated spectrum does not match the experimental one, especially in the spectral region around the dip structure. This finding suggests that the features on the scattering spectrum of a large Au nanorod supported on silicon should come from the interference between the different plasmon modes.

The Fano resonance in the large Au nanorods supported on silicon is further corroborated by analyzing the experimental scattering spectrum shown in Figure 3c with a phenomenological 3-pole Fano interference model[18,54,55]

$$S(E) = \left| a_r - \sum_{j=1}^{3} \frac{b_j \Gamma_j \exp(i\phi_j)}{E - E_j + i\Gamma_j} \right|^2 \quad (1)$$

where E is the photon energy, a_r is the background amplitude, b_j and ϕ_j specify the amplitude and phase of each resonance mode, and E_j and Γ_j represent the resonance energy and line width. Figure 4a illustrates the fitting result and the contribution of each resonance to the total signal. Excellent agreement is seen between the experimental scattering spectrum and the fitting with the parameters given in the caption. The model analysis provides important information for understanding the experimental spectrum. The dip structure is indeed induced by the coupling between a broad resonance at a higher energy of 2.15 eV (577 nm) and a narrow resonance at a lower energy of 2.00 eV (620 nm). The line widths of the two resonances are 0.20 eV (54 nm) and 0.09 eV (28 nm), respectively. By comparing the model analysis with the FDTD results shown in Figure 3c, we believe that these two resonances are the relative broad resonance at 2.30 eV (539 nm) excited under the V polarization scheme and the narrow resonance at 2.21 eV (561 nm) excited under the HL polarization scheme, respectively. Their line widths are 0.36 eV (66 nm) and 0.15 eV (38 nm), respectively. In order to support this conclusion, we further employed polarization dark-field scattering spectroscopy to study the scattering spectra of the large nanorods deposited on silicon under the different excitation polarizations.

The scattering spectra shown in Figures 2 and 3 were acquired with an unpolarized white-light source. The white-light illumination consists of both p- and s-polarized components. In order to achieve polarized excitation, we placed a linear polarizer and a pinhole after the light source and before the light is reflected into the dark-field objective (Figure S2, Supporting Information). The s- and p-polarized excitation light relative to the substrate plane can be realized by adjusting the height of the pinhole (see Experimental Section for the details). Under the s-polarized excitation, the HL and HT excitation polarization schemes can be implemented by rotating the substrate that carries

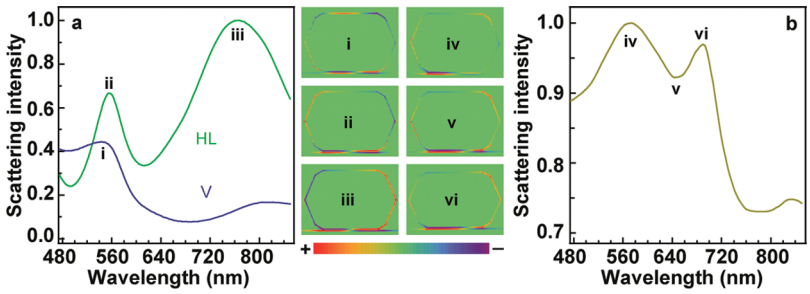

Figure 5. (a) Calculated scattering spectra of an individual large Au nanorod supported on the silicon substrate under the HL (green) and V (blue) excitation polarization schemes. (b) Calculated scattering spectrum of the large nanorod under p-polarized excitation. In the middle are shown the charge distributions associated with the different resonance modes (i−vi).

the large Au nanorods. The wavevector of the p-polarized excitation light is oriented at an angle of 53° from the substrate normal according to our dark-field excitation geometry. The p-polarized excitation contains both the normal and horizontal field components relative to the substrate plane. It cannot be decomposed experimentally into pure polarizations, but the horizontal field component can be adjusted to be along or perpendicular to the nanorod length axis by rotating the substrate. Figure 4b shows the experimental scattering spectra from an individual large Au nanorod supported on silicon under the HL, HT, and p-polarized excitation schemes, respectively. For this particular nanorod, the p-polarization is composed of the V and HL components. Clearly, the HL polarized excitation gives two scattering peaks. One is narrow and positioned at 540 nm, and the other is broad and centered at ~870 nm. Their line widths are 38 and 161 nm, respectively. Only a half portion of the scattering peak around 870 nm is observed due to the spectral limit of our optical system. The HT polarized excitation produces only a broad resonance peak with a much lower intensity. The contribution from the HT polarized excitation is therefore neglected in the following discussion. The resonance peaks observed under the HL and HT excitation polarizations are in very good agreement with those obtained from the FDTD calculations (Figure 3c). The deviation in the resonance wavelength of the HL-excited, low-energy mode is believed to arise from the inhomogeneous size distribution of the nanorod sample. In the calculations, only a nanorod with an average size is considered, while the individual nanorods are probed in the experiments. Under the p-polarized excitation that contains both the V and HL components, the scattering spectrum appears very similar to the experimental one shown in Figure 4a. A clear Fano resonance dip can be seen. The results from the polarization-dependent scattering spectroscopy are consistent with our above conclusion that the Fano resonance arises from the interference between the HL- and V-excited plasmon modes. The occurrences of the strong resonance mode along the vertical direction and the quadrupolar mode along the nanorod length axis are both enabled by the large dielectric constant of the silicon substrate.

We obtained from FDTD calculations the charge distributions (Figure 5) associated with the different plasmon modes in the large Au nanorod supported on silicon to reveal more clearly the origin of the observed Fano resonance. The HL-excited plasmon resonance at 770 nm (iii) is a dipolar mode, and the HL-excited resonance at 560 nm (ii) is a quadrupolar mode. The V-excited resonance at 540 nm (i) is complicated. It has an octupolar nature. The higher-order resonance modes are usually observable in metal nanocrystals of large sizes because of the retardation effect.[56,57] In addition, the invisibility of the HL-excited quadrupolar mode for the large Au nanorod supported on glass suggests that the large dielectric constant of silicon contributes to the observation of this resonance mode. Most importantly, all of these three resonance modes induce a similar image charge distribution that has a dipolar nature in the substrate. The same image charge distribution in the substrate leads to the effective hybridization among the three modes through Coulomb interactions. We also calculated the scattering spectrum and the charge distributions of the large Au nanorod on silicon under p-polarized excitation, with the horizontal field component oriented along the nanorod length axis (Figure 5). The scattering intensity difference between the calculated and experimental spectra under p-polarized excitation comes from the fact that the light scattered in all directions is taken during the calculation, while only the light scattered within the solid angle subtended by the objective is collected in the measurement. The charge distributions under p-polarized excitation show clearly again how the hybridization occurs. The resonance at 570 nm (iv) has an octupolar nature, while the resonance at 690 nm (vi) has a quadrupolar nature. These results indicate that the two resonances arise from the hybridization between the HL-excited quadrupolar mode and the V-excited octupolar mode. This finding is consistent with those from two recent theoretical studies, which show that strong substrate-mediated interaction leads to the hybridization between the dipolar and quadrupolar modes of a Au nanoshell or

a Ag nanocube.[37,41] Since the line width (39 nm) of the HL-excited quadrupolar mode is narrower than that (84 nm) of the V-excited octupolar mode, the coupling between a broad and a narrow mode with a similar resonance energy can induce Fano resonance and give rise to the dip structure in the scattering spectrum. This is also confirmed by the charge distribution at the dip position (v), which is quadrupole-dominant. In addition, we also calculated the absorption spectrum of the large nanorod supported on silicon (Figure S3, Supporting Information). A broad absorption peak is clearly seen at the same spectral position as the Fano dip on the scattering spectrum. Since a Fano dip on a scattering spectrum usually corresponds to a peak on the absorption spectrum,[23,25] the occurrence of the broad absorption peak on the calculated absorption spectrum is consistent with the observation of the Fano resonance on the scattering spectrum. On the other hand, we note that the Fano dip appears around 640 nm, which is at the red side of the quadrupolar and octupolar modes shown in Figure 5a. The deviation is ascribed to the hybridization between the quadrupolar and octupolar modes, which are excited simultaneously under p-polarized excitation. Owing to their spectral overlap, they can hybridize with each other through the image charges induced in the substrate. Once the interference occurs, new hybridized plasmon modes with different energies will be formed.[38] As a result, the Fano dip will appear at a different wavelength from those of the intrinsic quadrupolar and octupolar modes. Taken together, both the experimental measurements and theoretical analyses reveal that Fano resonance can be induced by depositing Au nanocrystals of large sizes on substrates with high dielectric constants.

The coupling between the large Au nanorods and the silicon substrate is through Coulomb interaction, which is strongly dependent on the nanorod−substrate spacing. We therefore further investigated the effect of the spacing on the observed Fano resonance. Mesostructured silica coatings were utilized as the spacers between the nanorods and silicon substrates. Because the dielectric constant of mesostructured silica is smaller than that of glass,[58] the use of the coating as the spacer does not notably affect the coupling between the nanorods and silicon substrate. Mesostructured silica coatings with five different thicknesses were fabricated. They are 2.7 ± 1.2, 4.8 ± 1.0, 7.6 ± 0.8, 14 ± 2, and 97 ± 9 nm, respectively. Figure 6a shows the representative scattering spectra of the large Au nanorods supported on the silicon substrates with the mesostructured silica coatings. As the thickness of the silica coating and thus the spacing between the nanorod and silicon substrate gets larger, the HL-excited dipole mode shifts to shorter wavelengths gradually. Its intensity also rises and becomes dominant in the overall scattering spectrum. The hybridized

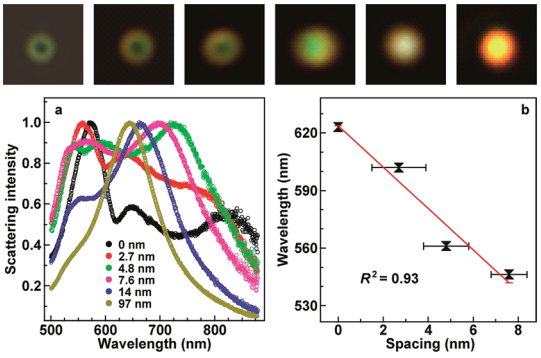

Figure 6. (a) Scattering spectra of the large Au nanorods supported on the silicon substrates that are coated with mesostructured silica films of different thicknesses: 0 nm (black), 2.7 ± 1.2 nm (red), 4.8 ± 1.0 nm (green), 7.6 ± 0.8 nm (purple), 14 ± 2 nm (blue), and 97 ± 9 nm (yellow). (b) Dependence of the position of the Fano dip on the thickness of the mesostructured silica film. The red line is a linear fit of the experimental data. The colored images at the top from left to right show the respective scattering patterns of the individual large nanorods supported on the silicon substrates that are coated with mesostructured silica films of the different thicknesses.

resonances associated with the HL-excited quadrupolar mode and V-excited octupolar mode shift slightly toward shorter wavelengths and broaden gradually. The dip first becomes shallower and then fades out when the nanorod−substrate spacing is larger than ~8 nm. When the spacing reaches 97 nm, the scattering spectrum of the large Au nanorod becomes similar to that of the large nanorod deposited on glass (Figure 3b). At the same time, the scattering pattern evolves from a green doughnut shape into an orange solid bright spot (Figure 6, top row). As has been explained in our previous report,[52] the evolution of the scattering pattern versus the nanorod−substrate spacing indicates the weakening of the coupling between the nanorod and silicon substrate. These findings confirm that the coupling between large Au nanorods and high-dielectric-constant substrates is very sensitive to the spacing. Moreover, the observation of the dip structure only when the spacing is less than ~8 nm implies that the hybridization between the different resonance modes in the nanorod mediated by the substrate is a near-field interaction. In order to quantify the dependence of the Fano resonance on the spacing, we plotted the dip position as a function of the coating thickness in Figure 6b. The dip position is seen to shift nearly linearly with the thickness. A linear fitting gives a slope of 11 nm (wavelength)/nm (spacing). This spacing sensitivity based on the Fano resonance is twice that found in a previous study on the basis of the plasmon coupling between a spherical Au nanocrystal and a flat Au film.[59] We therefore believe that the Fano resonance exhibited by large metal nanocrystals supported on high-dielectric-constant substrates can be potentially utilized for the design of sensing devices for ultrasensitively monitoring nanoscale distance changes.

CONCLUSIONS

We have successfully observed Fano resonance in individual Au nanorods supported on silicon substrates. Our study shows that multipolar plasmon modes can be effectively excited only when a Au nanorod with a large enough size is brought in close proximity to a substrate of very high dielectric constant. The strong image charges induced by the adjacent substrate mediate the hybridization between the different plasmon modes and give rise to rich scattering features from the nanorod. Specifically, the quadrupolar resonance mode excited along the nanorod length axis hybridizes with the vertically excited octupolar resonance mode to produce the Fano resonance. The position of the dip structure arising from the Fano resonance is linearly dependent on the nanorod−substrate spacing, with a slope of 11 nm (wavelength)/nm (spacing). The Fano resonance fades out gradually as the spacing is increased above ~8 nm. We believe that our findings provide a facile and effective platform for realizing Fano resonances in plasmonic metal nanostructures. In addition, they can also help in deepening our understanding of the localized surface plasmon resonances of metal nanocrystals situated in non-uniform dielectric environments. Moreover, the dependence of the Fano resonance dip on the nanorod−substrate spacing can be potentially employed for the development of plasmonic sensors for monitoring nanoscale distance changes.

EXPERIMENTAL SECTION

Growth of the Au Nanorods. The Au nanorod samples were obtained from NanoSeedz. They were prepared using a seed-mediated method together with anisotropic oxidation. Specifically, for the growth of the small nanorod sample, the seed solution was made by injecting a freshly prepared, ice-cold aqueous $NaBH_4$ solution (0.01 M, 0.6 mL) into an aqueous mixture composed of $HAuCl_4$ (0.01 M, 0.25 mL) and CTAB (0.1 M, 9.75 mL), followed by rapid inversion mixing for 2 min. The resultant seed solution was kept at room temperature for more than 2 h before use. The growth solution was made by the sequential addition of aqueous $HAuCl_4$ (0.01 M, 2 mL), $AgNO_3$ (0.01 M, 0.4 mL), HCl (1.0 M, 0.8 mL), and ascorbic acid (0.1 M, 0.32 mL) solutions into an aqueous CTAB (0.1 M, 40 mL) solution. The resultant solution was mixed by swirling for 30 s. After the seed solution was diluted 10 times with deionized water, 0.15 mL of the diluted seed solution was injected into the growth solution. The resultant reaction solution was gently mixed by inversion for 2 min and then left undisturbed overnight. The as-grown nanorod solution had a longitudinal plasmon wavelength of 740 nm. Ten milliliters of the obtained nanorod solution was then subjected to anisotropic oxidation by adding HCl (1.0 M, 0.2 mL) and H_2O_2 (30 wt %, 0.05 mL). The oxidation process was monitored by measuring the extinction spectra of the nanorod solution from time to time. When the longitudinal plasmon wavelength reached the desired value, the nanorods were washed by two cycles of centrifugation (4100*g*, 10 min) and redispersed in 0.1 M CTAB solutions to remove excess reactants. The growth of the large Au nanorod sample was similar to the procedure described above for the nanorod sample with a longitudinal plasmon wavelength of 740 nm, except that the amount of the seed solution was changed from 150 μL (10 times diluted) to 10 μL (50 times diluted).

Coating the Silicon Wafers with Mesostructured Silica Films of Varying Thicknesses. The mesostructured silica films of different thicknesses were coated onto the silicon wafers using the evaporation-induced self-assembly technique through dip coating.[60] For the coating of the films with thicknesses of 97 and 14 nm, poly(ethylene oxide)−poly(propylene oxide)−poly(ethylene oxide) triblock copolymer ($EO_{20}PO_{70}EO_{20}$, P123, 0.276 g) was first dissolved in ethanol (21.6 g). Tetraethyl orthosilicate (TEOS, 1.04 g) was prehydrolyzed in a solution containing dilute HCl (pH = 2, 0.54 g) and ethanol (1.2 g) by vigorous stirring at room temperature for 30 min. These two solutions were thereafter mixed together. The final molar composition of the precursor solution was 1 TEOS/0.0095 P123/6 H_2O/0.001 HCl/104.4 ethanol. After the precursor solution was stirred for 2 h at room temperature, they were dip-coated onto the silicon wafers at a speed of 10 mm·min^{-1}. The precursor solutions for the films with thicknesses of 7.6, 4.8, and 2.7 nm were similar, except that they were diluted 4, 8, and 16 times with ethanol, respectively. The dip-coating procedure was repeated four times for coating the thickest film while conducted only one time for the other four films. For the thickest film, the consecutive layers were coated after the previous layer was dried at room temperature for 1 h. The resultant silica films were dried at room temperature overnight before use.

Instrumentation. SEM imaging was performed on an FEI Quanta 400 FEG microscope. The thickness of the mesostructured silica coatings was measured on an atomic force microscope (Veeco Instruments, Veeco MultiMode). The scattering spectra of the individual Au nanorods were recorded on a dark-field optical microscope (Olympus BX60) that was integrated with a quartz−tungsten−halogen lamp (100 W), a monochromator (Acton SpectraPro 2300i), and a charge-coupled device camera (Princeton Instruments Pixis 512B). The camera was thermoelectrically cooled to −70 °C during the measurements. A dark-field objective (100×, numerical aperture = 0.80) was employed for both illuminating the nanorods with the white light and collecting the scattered light. The scattering spectrum from an individual nanorod was corrected by first subtracting the background spectrum taken from the adjacent region without Au nanorods and then dividing it with the calibrated response curve of the entire optical system. In addition to the scattering spectra recorded with the Princeton Instruments camera, color scattering images were also captured by use of a color digital camera (Carl Zeiss, AxioCam MRC5). Polarization-dependent scattering spectra were measured on the individual nanorods by placing a linear polarizer (U-AN360 Olympus, JAPAN) in the optical path right after the white-light source (Figure S2, Supporting Information). The polarization axis of the polarizer was aligned horizontally. In order to obtain a clean polarization at the substrate plane, a pinhole with a diameter of ~5 mm was inserted in the optical path right after the polarizer. The pinhole was used to select only one portion of the white-light beam that was then reflected at a particular position of the circular mirror. The s- and p-polarized incident light relative to the substrate plane was then achieved by adjusting the height of the pinhole. In our experiments, when the incident light was adjusted to be s-polarized with respect to the substrate plane, the HL and HT excitation polarization schemes were further realized by rotating the substrate according to the scribed marks on the substrate. The orientation of the nanorod relative to the scribed marks was determined beforehand by SEM imaging.

FDTD Calculations. The FDTD calculations were performed using FDTD Solutions 6.0, which was developed by Lumerical Solutions, Inc. During the calculations, an electromagnetic pulse in the wavelength range from 500 to 900 nm was launched into a box containing the target Au nanorod to simulate a propagating

plane wave interacting with the nanorod. The Au nanorod and its surrounding space were divided into 0.5 nm meshes. The refractive index of the medium in the top and side regions was taken to be 1.0 and that in the bottom was set according to the dielectric functions of the glass and silicon substrates. For the glass substrate, the refractive index is 1.55. For the silicon substrate, the refractive index with both real and imaginary parts was calculated from its dielectric function.[49] The small nanorod was modeled as a cylinder capped with a hemisphere at each end. Its size was set to be the same as the average size measured from the SEM images. The large nanorod was modeled according to an elongated tetrahexahedron, which has been described previously by us.[53] The sizes were set according to the TEM measurements. The different excitation polarizations were considered by setting the electric field being in the substrate plane either parallel or perpendicular to the nanorod length axis, as well as being vertical to the substrate. For p-polarized excitation, a plane wave with an incident angle of 53° relative to the substrate normal was introduced. The field component in the substrate plane was set to be oriented along the nanorod length axis. The charge distributions were obtained according to the electric field distributions at the different resonance modes. They were calculated on the cross-sectional plane that passes through the nanorod length axis and perpendicular to the substrate. In order to avoid the artificial scattering signals from the substrate, we set up the geometry (Figure S4, Supporting Information) of the substrate in our FDTD simulations according to what has been suggested in a recent study for optimally observing the scattering spectra of supported metal nanostructures.[37] Specifically, the substrate was penetrated through the perfectly matched layer of the simulation region so that the Fabry–Perot interference in the substrate can be eliminated. In addition, in order to avoid the reflection of the scattering light from the simulation boundary, the distance between the substrate surface and the bottom side of the simulation boundary was set to be 5 times the diameter of the nanorod. Because the spacing between the nanorod surface and the substrate is only 0.5 nm in our study, the source as well as the monitors used to collect the scattering intensity were extended in the substrate. The separation between the source boundary and the nanorod surface was 10 meshes. The same value was also used for the separation between the source boundary and the monitors.

Acknowledgment. This work was supported by the RGC GRF grant (Ref. No. CUHK403409, Project Code 2160391), the MOST of China (Grant No. 2011CB922200), and the RGC Direct Allocation (Project Code 2060417).

Supporting Information Available: The dark-field scattering images of the small and large Au nanorods deposited on the glass and silicon substrates, and the schematic of the optical setup for polarization-dependent dark-field scattering spectroscopy. This material is available free of charge *via* the Internet at http://pubs.acs.org.

REFERENCES AND NOTES

1. Young, T. The Bakerian Lecture: Experiments and Calculations Relative to Physical Optics. *Philos. Trans. R. Soc.* **1804**, *94*, 1–16.
2. Fano, U. Effects of Configuration Interaction on Intensities and Phase Shifts. *Phys. Rev.* **1961**, *124*, 1866–1878.
3. Garrido Alzar, C. L.; Martinez, M. A. G.; Nussenzveig, P. Classical Analog of Electromagnetically Induced Transparency. *Am. J. Phys.* **2002**, *70*, 37–41.
4. Miroshnichenko, A. E.; Flach, S.; Kivshar, Y. S. Fano Resonances in Nanoscale Structures. *Rev. Mod. Phys.* **2010**, *82*, 2257–2298.
5. Luk'yanchuk, B.; Zheludev, N. I.; Maier, S. A.; Halas, N. J.; Nordlander, P.; Giessen, H.; Chong, C. T. The Fano Resonance in Plasmonic Nanostructures and Metamaterials. *Nat. Mater.* **2010**, *9*, 707–715.
6. Madden, R. P.; Codling, K. New Autoionizing Atomic Energy Levels in He, Ne, and Ar. *Phys. Rev. Lett.* **1963**, *10*, 516–518.
7. Piao, G.; Lewis, R. A.; Fisher, P. Fano Resonances in the Absorption Spectrum of Singly Ionized Zinc in Germanium. *Solid State Commun.* **1990**, *75*, 835–838.
8. Gippius, N. A.; Tikhodeev, S. G.; Ishihara, T. Optical Properties of Photonic Crystal Slabs with an Asymmetrical Unit Cell. *Phys. Rev. B* **2005**, *72*, 045138.
9. Xu, Y.; Li, Y.; Lee, R. K.; Yariv, A. Scattering-Theory Analysis of Waveguide–Resonator Coupling. *Phys. Rev. E* **2000**, *62*, 7389–7404.
10. Tomita, M.; Totsuka, K.; Hanamura, R.; Matsumoto, T. Tunable Fano Interference Effect in Coupled-Microsphere Resonator-Induced Transparency. *J. Opt. Soc. Am. B* **2009**, *26*, 813–818.
11. Li, B.-B.; Xiao, Y.-F.; Zou, C.-L.; Liu, Y.-C.; Jiang, X.-F.; Chen, Y.-L.; Li, Y.; Gong, Q. H. Experimental Observation of Fano Resonance in a Single Whispering-Gallery Microresonator. *Appl. Phys. Lett.* **2011**, *98*, 021116.
12. Kroner, M.; Govorov, A. O.; Remil, S.; Biedermann, B.; Seidl, S.; Badolato, A.; Petroff, P. M.; Zhang, W.; Barbour, R.; Gerardot, B. D.; *et al.* The Nonlinear Fano Effect. *Nature* **2008**, *451*, 311–314.
13. Faist, J.; Capasso, F.; Sirtori, C.; West, K. W.; Pfeiffer, L. N. Controlling the Sign of Quantum Interference by Tunnelling from Quantum Wells. *Nature* **1997**, *390*, 589–591.
14. Bar-Ad, S.; Kner, P.; Marquezini, M. V.; Mukamel, S.; Chemla, D. S. Quantum Confined Fano Interference. *Phys. Rev. Lett.* **1997**, *78*, 1363–1366.
15. Göres, J.; Goldhaber-Gordon, D.; Heemeyer, S.; Kastner, M. A.; Shtrikman, H.; Mahalu, D.; Meirav, U. Fano Resonances in Electronic Transport through a Single-Electron Transistor. *Phys. Rev. B* **2000**, *62*, 2188–2194.
16. Chu, M.-W.; Myroshnychenko, V.; Chen, C. H.; Deng, J.-P.; Mou, C.-Y.; García de Abajo, F. J. Probing Bright and Dark Surface-Plasmon Modes in Individual and Coupled Noble Metal Nanoparticles Using an Electron Beam. *Nano Lett.* **2009**, *9*, 399–404.
17. Hao, F.; Sonnefraud, Y.; Van Dorpe, P.; Maier, S. A.; Halas, N. J.; Nordlander, P. Symmetry Breaking in Plasmonic Nanocavities: Subradiant LSPR Sensing and a Tunable Fano Resonance. *Nano Lett.* **2008**, *8*, 3983–3988.
18. Hao, F.; Nordlander, P.; Sonnefraud, Y.; Van Dorpe, P.; Maier, S. A. Tunability of Subradiant Dipolar and Fano-Type Plasmon Resonances in Metallic Ring/Disk Cavities: Implications for Nanoscale Optical Sensing. *ACS Nano* **2009**, *3*, 643–652.
19. Tribelsky, M. I.; Luk'yanchuk, B. S. Anomalous Light Scattering by Small Particles. *Phys. Rev. Lett.* **2006**, *97*, 263902.
20. Pakizeh, T.; Langhammer, C.; Zorić, I.; Apell, P.; Käll, M. Intrinsic Fano Interference of Localized Plasmons in Pd Nanoparticles. *Nano Lett.* **2009**, *9*, 882–886.
21. Mukherjee, S.; Sobhani, H.; Lassiter, J. B.; Bardhan, R.; Nordlander, P.; Halas, N. J. Fanoshells: Nanoparticles with Built-in Fano Resonances. *Nano Lett.* **2010**, *10*, 2694–2701.
22. Sonnefraud, Y.; Verellen, N.; Sobhani, H.; Vandenbosch, G. A. E.; Moshchalkov, V. V.; Van Dorpe, P.; Nordlander, P.; Maier, S. A. Experimental Realization of Subradiant, Superradiant, and Fano Resonances in Ring/Disk Plasmonic Nanocavities. *ACS Nano* **2010**, *4*, 1664–1670.
23. Mirin, N. A.; Bao, K.; Nordlander, P. Fano Resonances in Plasmonic Nanoparticle Aggregates. *J. Phys. Chem. A* **2009**, *113*, 4028–4034.
24. Fan, J. A.; Wu, C.; Bao, K.; Bao, J. M.; Bardhan, R.; Halas, N. J.; Manoharan, V. N.; Nordlander, P.; Shvets, G.; Capasso, F. Self-Assembled Plasmonic Nanoparticle Clusters. *Science* **2010**, *328*, 1135–1138.
25. Fan, J. A.; Bao, K.; Wu, C.; Bao, J. M.; Bardhan, R.; Halas, N. J.; Manoharan, V. N.; Shvets, G.; Nordlander, P.; Capasso, F. Fano-like Interference in Self-Assembled Plasmonic Quadrumer Clusters. *Nano Lett.* **2010**, *10*, 4680–4685.
26. Lassiter, J. B.; Sobhani, H.; Fan, J. A.; Kundu, J.; Capasso, F.; Nordlander, P.; Halas, N. J. Fano Resonances in Plasmonic Nanoclusters: Geometrical and Chemical Tunability. *Nano Lett.* **2010**, *10*, 3184–3189.
27. Hentschel, M.; Saliba, M.; Vogelgesang, R.; Giessen, H.; Alivisatos, A. P.; Liu, N. Transition from Isolated to Collective Modes in Plasmonic Oligomers. *Nano Lett.* **2010**, *10*, 2721–2726.

28. Zhang, S.; Genov, D. A.; Wang, Y.; Liu, M.; Zhang, X. Plasmon-Induced Transparency in Metamaterials. *Phys. Rev. Lett.* **2008**, *101*, 047401.
29. Verellen, N.; Sonnefraud, Y.; Sobhani, H.; Hao, F.; Moshchalkov, V. V.; Van Dorpe, P.; Nordlander, P.; Maier, S. A. Fano Resonances in Individual Coherent Plasmonic Nanocavities. *Nano Lett.* **2009**, *9*, 1663–1667.
30. Habteyes, T. G.; Dhuey, S.; Cabrini, S.; Schuck, P. J.; Leone, S. R. Theta-Shaped Plasmonic Nanostructures: Bringing "Dark" Multipole Plasmon Resonances into Action *via* Conductive Coupling. *Nano Lett.* **2011**, *11*, 1819–1825.
31. Verellen, N.; Van Dorpe, P.; Huang, C. J.; Lodewijks, K.; Vandenbosch, G. A. E.; Lagae, L.; Moshchalkov, V. V. Plasmon Line Shaping Using Nanocrosses for High Sensitivity Localized Surface Plasmon Resonance Sensing. *Nano Lett.* **2011**, *11*, 391–397.
32. Liu, N.; Langguth, L.; Weiss, T.; Kästel, J.; Fleischhauer, M.; Pfau, T.; Giessen, H. Plasmonic Analogue of Electromagnetically Induced Transparency at the Drude Damping Limit. *Nat. Mater.* **2009**, *8*, 758–762.
33. Dicken, M. J.; Aydin, K.; Pryce, I. M.; Sweatlock, L. A.; Boyd, E. M.; Walavalkar, S.; Ma, J.; Atwater, H. A. Frequency Tunable Near-Infrared Metamaterials Based on VO_2 Phase Transition. *Opt. Express* **2009**, *17*, 18330–18339.
34. Sámson, Z. L.; MacDonald, K. F.; Angelis, F. D.; Gholipour, B.; Knight, K.; Huang, C. C.; Fabrizio, E. D.; Hewak, D. W.; Zheludev, N. I. Metamaterial Electro-optic Switch of Nanoscale Thickness. *Appl. Phys. Lett.* **2010**, *96*, 143105.
35. Bachelier, G.; Russier-Antoine, I.; Benichou, E.; Jonin, C.; Del Fatti, N.; Vallée, F.; Brevet, P.-F. Fano Profiles Induced by Near-Field Coupling in Heterogeneous Dimers of Gold and Silver Nanoparticles. *Phys. Rev. Lett.* **2008**, *101*, 197401.
36. Yang, Z.-J.; Zhang, Z.-S.; Zhang, W.; Hao, Z.-H.; Wang, Q.-Q. Twinned Fano Interferences Induced by Hybridized Plasmons in Au–Ag Nanorod Heterodimers. *Appl. Phys. Lett.* **2010**, *96*, 131113.
37. Wu, Y. P.; Nordlander, P. Finite-Difference Time-Domain Modeling of the Optical Properties of Nanoparticles near Dielectric Substrates. *J. Phys. Chem. C* **2010**, *114*, 7302–7307.
38. Nordlander, P.; Prodan, E. Plasmon Hybridization in Nanoparticles near Metallic Surfaces. *Nano Lett.* **2004**, *4*, 2209–2213.
39. Le, F.; Lwin, N. Z.; Steele, J. M.; Käll, M.; Halas, N. J.; Nordlander, P. Plasmons in the Metallic Nanoparticle–Film System as a Tunable Impurity Problem. *Nano Lett.* **2005**, *5*, 2009–2013.
40. Knight, M. W.; Wu, Y. P.; Lassiter, J. B.; Nordlander, P.; Halas, N. J. Substrates Matter: Influence of an Adjacent Dielectric on an Individual Plasmonic Nanoparticle. *Nano Lett.* **2009**, *9*, 2188–2192.
41. Zhang, S. P.; Bao, K.; Halas, N. J.; Xu, H. X.; Nordlander, P. Substrate-Induced Fano Resonances of a Plasmonic Nanocube: A Route to Increased-Sensitivity Localized Surface Plasmon Resonance Sensors Revealed. *Nano Lett.* **2011**, *11*, 1657–1663.
42. Sherry, L. J.; Chang, S.-H.; Schatz, G. C.; Van Duyne, R. P.; Wiley, B. J.; Xia, Y. N. Localized Surface Plasmon Resonance Spectroscopy of Single Silver Nanocubes. *Nano Lett.* **2005**, *5*, 2034–2038.
43. Jain, P. K.; Lee, K. S.; El-Sayed, I. H.; El-Sayed, M. A. Calculated Absorption and Scattering Properties of Gold Nanoparticles of Different Size, Shape, and Composition: Applications in Biological Imaging and Biomedicine. *J. Phys. Chem. B* **2006**, *110*, 7238–7248.
44. Ni, W. H.; Kou, X. S.; Yang, Z.; Wang, J. F. Tailoring Longitudinal Surface Plasmon Wavelengths, Scattering and Absorption Cross Sections of Gold Nanorods. *ACS Nano* **2008**, *2*, 677–686.
45. Kou, X. S.; Ni, W. H.; Tsung, C.-K.; Chan, K.; Lin, H.-Q.; Stucky, G. D.; Wang, J. F. Growth of Gold Bipyramids with Improved Yield and Their Curvature-Directed Oxidation. *Small* **2007**, *3*, 2103–2113.
46. Sönnichsen, C.; Franzl, T.; Wilk, T.; von Plessen, G.; Feldmann, J.; Wilson, O.; Mulvaney, P. Drastic Reduction of Plasmon Damping in Gold Nanorods. *Phys. Rev. Lett.* **2002**, *88*, 077402.
47. Ming, T.; Kou, X. S.; Chen, H. J.; Wang, T.; Tam, H.-L.; Cheah, K.-W.; Chen, J.-Y.; Wang, J. F. Ordered Gold Nanostructure Assemblies Formed by Droplet Evaporation. *Angew. Chem., Int. Ed.* **2008**, *47*, 9685–9690.
48. Tsung, C.-K.; Kou, X. S.; Shi, Q. H.; Zhang, J. P.; Yeung, M. H.; Wang, J. F.; Stucky, G. D. Selective Shortening of Single-Crystalline Gold Nanorods by Mild Oxidation. *J. Am. Chem. Soc.* **2006**, *128*, 5352–5353.
49. Palik, E. D. *Handbook of Optical Constants of Solids*; Academic Press: Boston, MA, 1985.
50. Zhao, F.; Du, Y.-K.; Xu, J.-K.; Liu, S.-F. Determination of Surfactant Molecular Volume by Atomic Force Microscopy. *Colloid J.* **2006**, *68*, 784–787.
51. Sun, Z. H.; Ni, W. H.; Yang, Z.; Kou, X. S.; Li, L.; Wang, J. F. pH-Controlled Reversible Assembly and Disassembly of Gold Nanorods. *Small* **2008**, *4*, 1287–1292.
52. Chen, H. J.; Ming, T.; Zhang, S. R.; Jin, Z.; Yang, B. C.; Wang, J. F. Effect of the Dielectric Properties of Substrates on the Scattering Patterns of Gold Nanorods. *ACS Nano* **2011**, *5*, 4865–4877.
53. Ming, T.; Feng, W.; Tang, Q.; Wang, F.; Sun, L. D.; Wang, J. F.; Yan, C. H. Growth of Tetrahexahedral Gold Nanocrystals with High-Index Facets. *J. Am. Chem. Soc.* **2009**, *131*, 16350–16351.
54. Christ, A.; Ekinci, Y.; Solak, H. H.; Gippius, N. A.; Tikhodeev, S. G.; Martin, O. J. F. Controlling the Fano Interference in a Plasmonic Lattice. *Phys. Rev. B* **2007**, *76*, 201405(R).
55. Ropers, C.; Park, D. J.; Stibenz, G.; Steinmeyer, G.; Kim, J.; Kim, D. S.; Lienau, C. Femtosecond Light Transmission and Subradiant Damping in Plasmonic Crystals. *Phys. Rev. Lett.* **2005**, *94*, 113901.
56. Félidj, N.; Grand, J.; Laurent, G.; Aubard, J.; Lévi, G.; Hohenau, A.; Galler, N.; Aussenegg, F. R.; Krenn, J. R. Multipolar Surface Plasmon Peaks on Gold Nanotriangles. *J. Chem. Phys.* **2008**, *128*, 094702.
57. Hao, F.; Larsson, E. M.; Ali, T. A.; Sutherland, D. S.; Nordlander, P. Shedding Light on Dark Plasmons in Gold Nanorings. *Chem. Phys. Lett.* **2008**, *458*, 262–266.
58. Yang, P. D.; Wirnsberger, G.; Huang, H. C.; Cordero, S. R.; McGehee, M. D.; Scott, B.; Deng, T.; Whitesides, G. M.; Chmelka, B. F.; Buratto, S. K.; *et al.* Mirrorless Lasing from Mesostructured Waveguides Patterned by Soft Lithography. *Science* **2000**, *287*, 465–467.
59. Mock, J. J.; Hill, R. T.; Degiron, A.; Zauscher, S.; Chilkoti, A.; Smith, D. R. Distance-Dependent Plasmon Resonant Coupling between a Gold Nanoparticle and Gold Film. *Nano Lett.* **2008**, *8*, 2245–2252.
60. Zhao, L.; Ming, T.; Li, G. S.; Chen, H. J.; Wang, J. F.; Yu, J. C. Monosteps on the Surfaces of Mesostructured Silica and Titania Thin Films. *Small* **2010**, *6*, 1880–1885.